

MIT Open Access Articles

*FERMI -LAT OBSERVATIONS OF
SUPERNOVA REMNANTS KESTEVEN 79*

The MIT Faculty has made this article openly available. *Please share*
how this access benefits you. Your story matters.

Citation: Auchettl, Katie, Patrick Slane, and Daniel Castro. "FERMI -LAT OBSERVATIONS OF SUPERNOVA REMNANTS KESTEVEN 79 ." The Astrophysical Journal 783, no. 1 (February 10, 2014): 32. © 2014 The American Astronomical Society

As Published: <http://dx.doi.org/10.1088/0004-637X/783/1/32>

Publisher: IOP Publishing

Persistent URL: <http://hdl.handle.net/1721.1/93164>

Version: Final published version: final published article, as it appeared in a journal, conference proceedings, or other formally published context

Terms of Use: Article is made available in accordance with the publisher's policy and may be subject to US copyright law. Please refer to the publisher's site for terms of use.



FERMI-LAT OBSERVATIONS OF SUPERNOVA REMNANTS KESTEVEN 79

KATIE AUCHETTL^{1,2,3,4}, PATRICK SLANE¹, AND DANIEL CASTRO⁵

¹ Harvard-Smithsonian Center for Astrophysics, 60 Garden Street, Cambridge, MA 02138, USA

² School of Physics, Monash University, Melbourne, Victoria 3800, Australia

³ Monash Centre for Astrophysics, Monash University, Victoria 3800, Australia

⁴ ARC Centre of Excellence for Particle Physics at the Tera-scale, Monash University, Victoria 3800, Australia

⁵ MIT-Kavli Center for Astrophysics and Space Research, 77 Massachusetts Avenue, Cambridge, MA 02139, USA

Received 2013 August 22; accepted 2014 January 6; published 2014 February 10

ABSTRACT

In this paper, we report on the detection of γ -ray emission coincident with the Galactic supernova remnant (SNR) Kesteven 79 (Kes 79). We analyzed approximately 52 months of data obtained with the Large Area Telescope on board the *Fermi Gamma-ray Space Telescope*. Kes 79 is thought to be interacting with adjacent molecular clouds, based on the presence of strong $^{12}\text{CO } J = 1 \rightarrow 0$ and $\text{HCO}^+ J = 1 \rightarrow 0$ emission and the detection of 1720 MHz line emission toward the east of the remnant. Acceleration of cosmic rays is expected to occur at SNR shocks, and SNRs interacting with dense molecular clouds provide a good testing ground for detecting and analyzing the production of γ -rays from the decay of π^0 into two γ -ray photons. This analysis investigates γ -ray emission coincident with Kes 79, which has a detection significance of $\sim 7\sigma$. Additionally, we present an investigation of the spatial and spectral characteristics of Kes 79 using multiple archival *XMM-Newton* observations of this remnant. We determine the global X-ray properties of Kes 79 and estimate the ambient density across the remnant. We also performed a similar analysis for Galactic SNR Kesteven 78 (Kes 78), but due to large uncertainties in the γ -ray background model, no conclusion can be made about an excess of GeV γ -ray associated with the remnant.

Key words: gamma rays; ISM – ISM: individual objects (Kesteven 79, G33.6+0.1, Kesteven 78, G32.8–0.1) – ISM: supernova remnants

Online-only material: color figures

1. INTRODUCTION

Supernova remnants (SNRs) have long been regarded as efficient accelerators of Galactic cosmic rays (CRs). As predicted by diffusive shock acceleration, the shock front of an SNR is expected to naturally accelerate electrons and ions with a power law momentum distribution (e.g., Malkov & O’C Drury 2001), which produces non-thermal emission from the SNR. The existence of this population of particles is inferred directly from γ -rays, while the nature of the γ -ray emission and the efficiency of the particle acceleration is characterized using observations in multiple wavelengths. Non-thermal X-ray emission from a number of SNRs such as SN 1006 (Koyama et al. 1995; Reynolds 1998), Vela Jr. (Aschenbach 1998), RX J1713.7–3946 (Uchiyama et al. 2007), and Tycho (Warren et al. 2005) has established that a population of relativistic electrons can be accelerated to TeV energies at SNR shocks. Ground-based measurements of TeV γ -ray emission from SNRs such as Tycho (Acciari et al. 2011; Morlino & Caprioli 2012) suggest that there is a population of particles that are being accelerated to energies approaching the knee ($E_{\text{knee}} \sim 10^{15}$ eV) of the CR energy spectrum. Even with this evidence, there has been an ongoing debate in the literature (reviewed in Reynolds 2008) as to whether this γ -ray emission arises from relativistic hadrons interacting with the ambient medium (hadronic in origin), inverse Compton scattering, or non-thermal bremsstrahlung emission from high-energy electrons (leptonic origin).

Gamma-rays can be produced from the decay of a neutral pion into two photons. This decay results from the interaction of relativistic ions with ambient material via proton–proton interactions (Claussen et al. 1997). The two γ -rays in the neutral pion’s rest frame have an energy of $\frac{1}{2}m_{\pi}c^2 = 67.5$ MeV, where m_{π} is the rest mass of π^0 and c is the speed of light. Molecular

clouds (MCs) are a large source of protons, hence SNRs that are known to be interacting with dense MCs provide effective targets for detecting and analyzing emission from accelerated hadrons. The interaction of an SNR’s shockwave with dense molecular material is often inferred from the detection of 1720 MHz hydroxyl (OH) masers in the direction of the SNR (Hewitt et al. 2009). Additionally, the combination of the detection of molecular line broadening and/or asymmetric profiles, the enhancement of excitation line ratios such as $J = 2 \rightarrow 1/J = 1 \rightarrow 0$, and the detection of [Fe II] or H_2 line emission due to rotational–vibrational coupling or morphological agreement of molecular features with SNR features all provide persuasive evidence for SNR–MC interactions (Chen et al. 2013).

Observations of GeV to TeV γ -rays allow one to identify π^0 -decay signatures that can provide information about the parent accelerated protons. Compared to other γ -ray telescopes such as the Energetic Gamma-Ray Experiment Telescope, the Large Area Telescope (LAT) on board the *Fermi Gamma-ray Space Telescope* has significantly improved the sensitivity and resolution in the MeV–GeV energy range, providing new opportunities for studying astrophysical objects such as SNRs. Since its launch, there have been multiple reports of the detection of GeV γ -ray emission from a large number of SNRs using data obtained from the *Fermi*-LAT, such as IC443 (Abdo et al. 2010b; Ackermann et al. 2013), W44 (Abdo et al. 2010a; Ackermann et al. 2013), W41, MSH17–39, G337.0–0.1 (Castro et al. 2013), G349.7–0.5, CTB 37A, 3C 391, G8.7–0.1 (Castro & Slane 2010), and Tycho (Giordano et al. 2012). Using these measurements, many authors have modeled the γ -ray spectra of these remnants to determine the mechanism behind this emission. However, it has been difficult to unequivocally establish whether the γ -ray emission arises from the interaction of relativistic protons with the surrounding ambient medium or

from inverse Compton or non-thermal bremsstrahlung emission. Observations of RX J1713.7–3946 using the *Fermi*-LAT have suggested that the γ -ray emission is dominated by leptonic processes (Ellison et al. 2010; Abdo et al. 2011). However, assuming that the SNR is interacting with a clumpy interstellar medium, Inoue et al. (2012) concluded that the γ -rays resulted from pion decay. Gamma-ray data from the *Fermi*-LAT has also been combined with other MeV-GeV observations, such as AGILE observations of SNR W44, which strongly suggested that π^0 -decay dominates the observed γ -ray emission (Giuliani et al. 2011). This conclusion was confirmed by Ackermann et al. (2013), who detected the characteristic pion-decay feature in the γ -ray spectra of W44 and IC443 using the *Fermi*-LAT.

Kes 79 (G33.6+0.1) is a Galactic SNR that was first discovered by Caswell et al. (1975) using the 408 MHz Molonglo and 5000 MHz Parkes radio continuum survey. The remnant appears to consist of two concentric incomplete radio shells with several short, bright radio filaments toward the center of the remnant (Velusamy et al. 1991; Frail & Clifton 1989). Using single-based line interferometry over a limited range of velocities, Caswell et al. (1975) produced an H I absorption spectrum in the direction of Kes 79, which was used to estimate a lower limit of 7 kpc for the kinematic distance. This distance estimate implies that the diameter of Kes 79 has a lower limit of 20 pc. This is several times the size of a young SNR (less than a thousand years old), implying that Kes 79 is at least several thousand years old (Green & Dewdney 1992). This conclusion was also obtained by Sun et al. (2004), who derived a Sedov age of 5.9–7.8 kyr using a shock temperature of 0.4–0.7 keV.

Using the Dominion Radio Astrophysical Observatory, Green (1989) detected an unusually broad 1667 MHz OH absorption feature coincident with Kes 79. It was found at a position $(\alpha_{J1950}, \delta_{J1950}) = (18^{\text{h}}50^{\text{m}}10^{\text{s}}, +00^{\circ}35'00'')$, with local standard of rest (LSR) velocity between +95 and +115 km s⁻¹. This absorption feature coincides with a nearby MC found at the same velocity, which suggests that the remnant's shock wave is interacting with this MC. The CO survey conducted by Scoville et al. (1987) reveals a large elongated MC at a velocity of 100 km s⁻¹ overlapping the eastern and southeastern region of Kes 79. The suggestion that Kes 79 is interacting with nearby MCs is also supported by the detection of extended, bright ¹²CO $J = 1 \rightarrow 0$ emission and strong HCO⁺ $J = 1 \rightarrow 0$ emission from the east and southeastern regions of Kes 79 at a velocity of 105 km s⁻¹ by using the NRAO 12 m telescope (Green & Dewdney 1992). As the mean hydrogen density of the MC associated with Kes 79 is much less than the density required to produce significant HCO⁺ emission, the authors suggested that the observed HCO⁺ emission arises from the interaction with the SNR shock. Using the Parkes telescope, Green et al. (1997) detected 1720 MHz line emission from Kes 79, while Zubrin & Shulga (2008) reported on the detection of a 95 GHz methanol maser. However, observations with the 12 m Arizona Radio Observatory and Very Large Array (VLA) failed to confirm the methanol maser detection (Frail 2011). These observations provide additional evidence for a kinematic distance of ~ 7 kpc.

Sun et al. (2004) used a 30 ks *Chandra* ACIS-I observation to reveal the rich structure of the X-ray emission of Kes 79, implying a complicated surrounding environment. There are many bright and faint X-ray filaments, three partial X-ray shells, a loop in the southwest and a “protrusion” toward the northeast. Nearly all of these spatial structures have a corresponding radio structure. Using the semi-analytic, thin-shell approximation

for an SNR shock crossing a density jump derived by Chen et al. (2003), Sun et al. (2004) derived an average value of 0.36 cm⁻³ for the ambient density. Using two 30 ks archival *XMM* observations, Giacani et al. (2009) derived a global X-ray spectrum, which indicated dominant emission from Mg, Si, S, and Fe, consistent with results derived using ASCA (Sun & Wang 2000; Tsunemi & Enoguchi 2002).

Kes 78 (G32.8–0.1) is a Galactic SNR that was first identified in a 408 MHz and 5000 MHz radio continuum survey by Kesteven (1968) and Caswell et al. (1975), respectively. It is an elongated shell type SNR that is 20' \times 10' in diameter and has a partially brightened non-thermal radio shell with a spectral index of -0.5 (Kassim 1992). In the literature, there are multiple estimates of the distance of Kes 78 using a number of different measurements, (e.g., Caswell et al. 1975; Allakhverdiev et al. 1983; Gosachinskii & Khersonskii 1985; Case & Bhattacharya 1998; Boumis et al. 2009; Xu & Zhang 2009). Zhou & Chen (2011) used H I absorption spectra at different LSR velocities and the association of Kes 78 with an MC at an LSR velocity of ~ 81 km s⁻¹ to derive a distance of 4.8 kpc. Gosachinskii & Khersonskii (1985), using H I observations, estimated the age of the remnant to be $\sim 1.2 \times 10^5$ yr.

Koralesky et al. (1998) detected a single, 86.1 km s⁻¹ 1720 MHz OH maser at a position of $(\alpha_{J2000}, \delta_{J2000}) = (18^{\text{h}}51^{\text{m}}48^{\text{s}}04, 00^{\circ}10'35'')$ using the VLA. This maser is coincident with the eastern edge of Kes 78's radio shell. The detection of this maser indicates that the SNR shock-wave is interacting with the surrounding MCs. Observations of ¹²CO reveal that Kes 78 is coincident with dense MCs found toward the east of the remnant where the OH maser emission arises (Zhou & Chen 2011). The distribution of ¹²CO traces out the eastern radio shell of the remnant and it indicates that Kes 78 is expanding into a CO cavity. Elevated ¹²CO $J = 2 \rightarrow 1$ / $J = 1 \rightarrow 0$ ratios along the boundary of the SNR also suggest the presence of perturbations in the molecular gas due to the interaction of the SNR shock (Zhou & Chen 2011). The kinematic distance to Kes 78 implied by the association of MCs is $4.8^{+3.1}_{-0.7}$ kpc.

Zhou & Chen (2011) detected X-rays arising from the northeastern region of the radio shell using *XMM-Newton*. This emission can be modeled using a low density, under-ionized plasma with a temperature of $kT \sim 1.5$ keV. The H.E.S.S. collaboration reported an extended very high energy (VHE) γ -ray source, HESS J1852–000, that could be associated with the eastern edge of the remnant interacting with a nearby molecular cloud or with a previously undiscovered pulsar-wind nebula (Kosack et al. 2011).⁶

In this paper, we study the γ -ray emission coincident with Kes 79 and Kes 78 and investigate the nature of this emission by modeling the broadband spectrum. Additionally, we perform a spatial and spectral analysis of archival *XMM* data for Kes 79 and report on the X-ray properties of this remnant. In Section 2, we describe how the *Fermi*-LAT data are analyzed and present the results of this analysis. In Section 3, we present our method and the results of our spatial and spectral analysis of archival *XMM* data for Kes 79, while in Section 4, we discuss the implication of the results obtained.

2. FERMI-LAT OBSERVATIONS OF SNR Kes 79 AND Kes 78

For this study, 52 months of data, collected from 2008 August to 2012 December using the *Fermi* Gamma-ray Space

⁶ <http://www.mpi-hd.mpg.de/hfm/HESS/pages/home/som/2011/02/>

Telescope Large Area Telescope (*Fermi*-LAT), were analyzed. As previously detailed in Ackermann et al. (2012), only events belonging to the “Pass7 V6” source class were selected for this study. Using this source class reduces the residual background of the data. We used the “Pass7 version 6” instrument response function (IRF), which was generated by using data recorded in-flight and incorporates effects that were not included in the pre-launch analysis such as accidental coincidence effects in the detectors (Ackermann et al. 2012). For the IRFs that we used in this analysis, the systematic uncertainties in the effective area of the *Fermi*-LAT are 10% at 100 MeV, decreasing to 5% at 560 MeV, and increasing to 10% at 10 GeV.⁷ To reduce the effect of terrestrial albedo γ -rays on the data, we selected events coming from zenith angles smaller than 100° . To further decrease the effects of these terrestrial γ -rays, we also excluded events that were detected when the rocking angle of the LAT was greater than 52° . The analysis included data from circular regions within a radius of 20° , centered on Kes 79 and Kes 78. The γ -ray data in the direction of Kes 79 and Kes 78 were analyzed using the Fermi Science Tools v9r27p1.⁸

To obtain morphological, positional, and spectral information about the remnant, the maximum likelihood fitting technique, *gtlike*, was used. Likelihood analysis was used on the *Fermi*-LAT data due to the low detection rates of γ -rays and the large point spread function (PSF) of the *Fermi*-LAT. *gtlike* calculates the parameters that best fit the emission model by maximizing the joint probability of the data, given a specific emission model (Mattox et al. 1996). *gtlike* uses diffuse Galactic and isotropic emission models to account for the γ -rays generated by CRs interacting with background photons, the interstellar medium, the extragalactic diffuse, and residual backgrounds. It also includes known γ -ray sources by placing them at fixed positions and calculating the background contribution from these sources to the data. The γ -ray emission from the Milky Way is described by the mapcube file `gal_2yearp7v6_v0.fits`, while the table `iso_p7v6source.txt` models the isotropic emission arising from extragalactic diffuse and residual backgrounds.⁹

2.1. Spatial Analysis

Gamma-ray data, with energy ranging from 2 to 200 GeV converted in the front section of the LAT, were selected to determine the spatial characteristics of the γ -ray emission from Kes 79 and Kes 78. These events were chosen as they improve the angular resolution of the data. The 1σ containment radius angle for front-selected photons in this energy band is $\leq 0.3^\circ$. Test statistic (TS) maps constructed using *gttmap* allow one to determine the detection significance as well as the position and extent of the source. The TS is defined as the logarithmic ratio of the likelihood of a point source being found at a given position on a spatial grid, to the likelihood of the model without the additional source, $2\log(L_{\text{ps}}/L_{\text{null}})$. The image resolution of these TS maps is defined by the size of the grid used for this analysis; we set the grid to be 0.05° .

To analyze the surrounding neighborhood of the remnant, we generated count maps of $1^\circ \times 1^\circ$ regions centered around Kes 79 and Kes 78. The count maps were smoothed by a

Gaussian of width similar to the PSF of the events selected and are presented in Figure 1. The radio emission from Kes 79 and Kes 78, as observed during the VLA Galactic plane survey, are overlaid as the green contours (Stil et al. 2006). Possibly associated with Kes 79 is an unresolved γ -ray source designated as 2FGL J1852.7+0047c in the *Fermi*-LAT Second Source Catalogue, while possibly associated with Kes 78 is an unresolved γ -ray source designated as 2FGL J1850.7–0014c. In the Second Source Catalogue, these two *Fermi*-LAT sources are characterized by photon power law indexes of $\Gamma = 2.53 \pm 0.21$ and $\Gamma = 2.85 \pm 0.18$, respectively. The photon flux of these sources over an energy of 1 GeV–100 GeV is $(1.8 \pm 0.5) \times 10^{-9}$ photons $\text{cm}^{-2} \text{s}^{-1}$ and $(4.3 \pm 0.9) \times 10^{-9}$ photons $\text{cm}^{-2} \text{s}^{-1}$, respectively. The position and extent of each of these γ -ray sources are plotted as a magenta circle, in Figure 1.

To determine the significance of the detection of the γ -ray emission from Kes 79 and Kes 78, we generated a TS map for each remnant. For Kes 79, we calculated the TS map over an energy range of 0.2–2 GeV and obtained a detection significance of $\sim 7\sigma$. The TS map is presented as the cyan contours overlaid in Figure 1(a). The TS contours suggest that the γ -ray emission in this region is associated with Kes 79. For Kes 78, we calculated a TS map over an energy range of 1 GeV–3.2 GeV and overlaid the TS map as cyan contours in Figure 1(b). We select this range, as the resolution of the *Fermi*-LAT below 1 GeV is significantly affected by the large uncertainty in the Galactic diffuse emission model. The TS contours do not show a concentration (or peak) of flux at the centroid of Kes 78, in contrast to the significant γ -ray emission seen in the region centered on Kes 79 (Figure 1(a)). The detection significance of ~ 5 – 6σ in the region of Kes 78 is equal to or less than the detection significance seen everywhere in the field of view, indicating that the observed γ -ray emission is dominated by uncertainties in the background model or by γ -ray emission spilling over from nearby sources. Thus, it is not possible to claim an excess of GeV γ -ray emission associated with the remnant.

2.2. Spectral Analysis

The spectral energy distribution characteristics of the *Fermi*-LAT emission coincident with Kes 79 are produced by using events with an energy of 0.2–200 GeV. This energy range is selected for multiple reasons, including avoiding source confusion, avoiding the large flux uncertainties that arise below 0.2 GeV due to limitations of the Galactic diffuse model, and reducing the influence that the rapidly changing effective area of the instrument at low energies has on the data. We perform the spectral analysis by modeling the flux at each energy bin and then estimate the parameters that best fit the data using the maximum likelihood technique *gtlike*. We also included in the likelihood fits background sources from the 24 month *Fermi*-LAT Second Source Catalogue (Nolan et al. 2012) that are found within a 20° circular region centered on Kes 79.¹⁰ For Kes 79, all evident background sources were identified in the *Fermi*-LAT Second Source Catalogue and the associated parameters from the catalog were used.

For each energy bin, the normalization of the diffuse Galactic component was left free to account for correlations between close-by sources. In addition to using the statistical uncertainties from the likelihood analysis, the systematic uncertainty associated with the Galactic diffuse emission was also considered by

⁷ <http://fermi.gsfc.nasa.gov/ssc/data/analysis/LATcaveats.html>

⁸ The Fermi Science Support Center has made publically available the Science Tools package and related documentation at <http://fermi.gsfc.nasa.gov/ssc>.

⁹ The most up to date `gal_2yearp7v6_v0.fits` and `iso_p7v6source.txt` were obtained from <http://fermi.gsfc.nasa.gov/ssc/data/access/lat/BackgroundModels.html>.

¹⁰ The data for these sources is made available by the Fermi Science Support Center and is found at http://fermi.gsfc.nasa.gov/ssc/data/access/lat/2yr_catalog/.

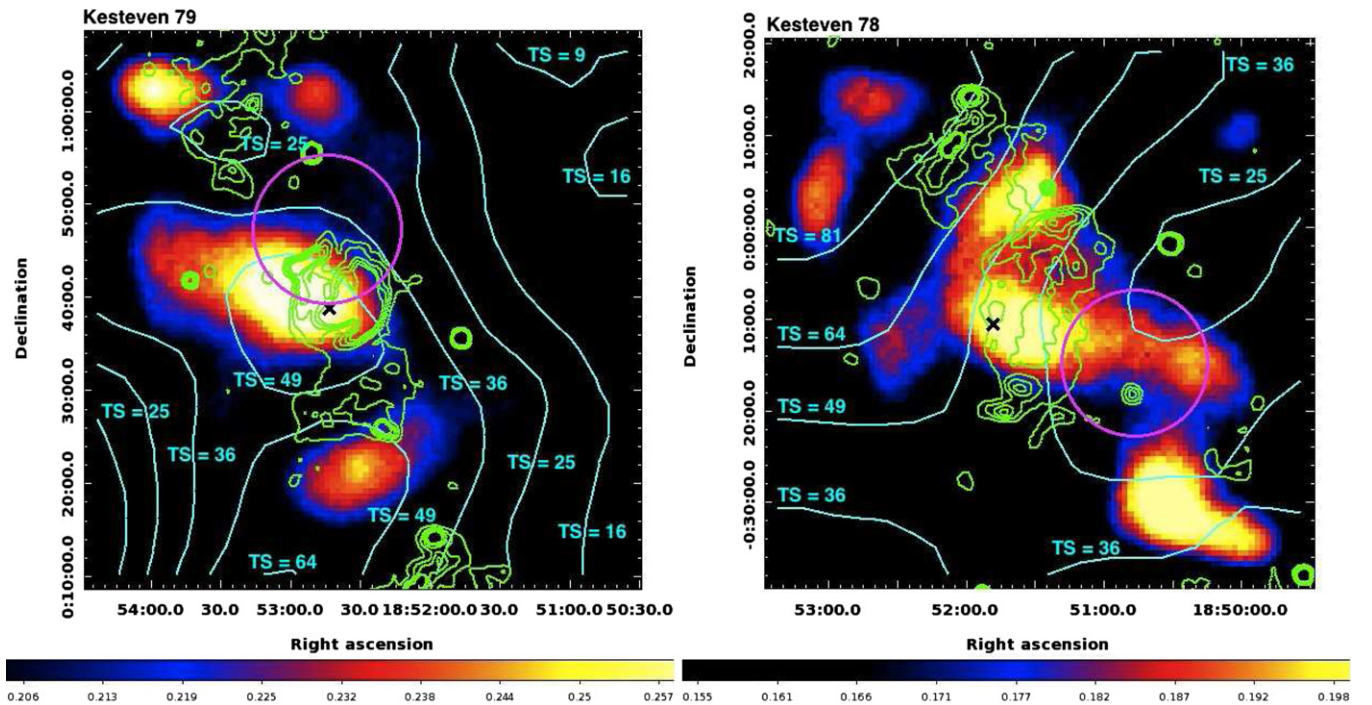


Figure 1. Smoothed *Fermi*-LAT count maps of events with energy of 2–200 GeV in a region $1^\circ \times 1^\circ$ surrounding Kes 79 and Kes 78, respectively (units are counts degree $^{-2}$). The pixel binning is 0:01 and the maps are smoothed with Gaussians of width 0.2 arcmin. The magenta circles correspond to the *Fermi*-LAT sources, 2FGL J1852.7+0047c and 2FGL J1850.7–0014c, located near Kes 79 and Kes 78, respectively. The radio emission observed during the VLA Galactic plane survey are overlaid as the green contours (Stil et al. 2006), while the *Fermi*-LAT TS map contours are shown in cyan. The square root of the TS value is approximately equal to the detection significance. The position of the 1667 MHz OH absorption feature for Kes 79 and the position of the 1720 MHz OH maser for Kes 78 are indicated by the black crosses. The scale corresponds to the number of counts degree $^{-2}$.

(A color version of this figure is available in the online journal.)

artificially altering the normalization of the Galactic background by $\pm 6\%$ from the best-fit value at each energy bin. This method is modeled from similar treatments presented in Castro & Slane (2010) and Castro et al. (2012).

The γ -ray spectrum of the *Fermi*-LAT sources coincident with Kes 79 is shown in Figure 2. Upper limits are plotted as blue triangles. The γ -ray spectrum of Kes 79 can be fitted using a simple power law with a spectral index of 2.6 ± 0.1 , while an exponential cut-off power law with $E_{\text{cut}} = 2.7 \pm 0.6$ GeV and a spectral index of 2.00 ± 0.4 significantly improves the fit. Assuming a distance of 7 kpc to Kes 79, the luminosity of this γ -ray source for an energy range of 0.1–100 GeV is 6.1×10^{35} erg s $^{-1}$. Both the simple power law and exponential cut-off models for Kes 79 are shown in Figure 2 as the green dotted and cyan dashed plots, respectively. The parameters that define these best fits, along with the detection significance and positional information of Kes 79, are summarized in Table 1.

3. XMM-NEWTON OBSERVATIONS AND ANALYSIS

For Kes 79 we analyzed 21 archival *XMM-Newton* observations which were found within a radius of 12 arcmin of the centroid of Kes 79 (see Table 2). These observations were performed over a period of five years and have an effective exposure time of ~ 447 ks and ~ 456 ks for the MOS1 and MOS2 detector, respectively. All *XMM-Newton* observations simultaneously acquired EPIC-MOS, and EPIC-pn observations, with the pn detector operating in “small window” mode, while the MOS cameras operated in “full frame” mode. For all observations, the full SNR was included in the field of view of the MOS cameras, while only part of the remnant was detected by

EPIC-pn due to it operating in “small window” mode. Thus for this analysis, we only used data from the MOS cameras.

Giacani et al. (2009) used the *XMM-Newton* observations 204970201 and 204970301 to compare the morphology of the X-ray emission and 324 MHz VLA observations of Kes 79, while Halpern & Gotthelf (2010) used the EPIC-pn observations of 16 of the *XMM-Newton* observations listed in Table 2 to perform a dedicated series of timing observations of PSR J1852+0040 found in Kes 79. We re-analyzed all 21 archival EPIC MOS observations previously presented in the literature using the *XMM-Newton* Science Analysis System (SAS) version 12.0.1 and the most up to date calibration files.¹¹ All analyses were completed by starting from the observational data files. For the MOS cameras, we selected single to quadruple patterned events. For both spectral and imaging analysis, all event files were filtered such that all flagged events were removed and periods of high background and/or photon flare contamination were removed as suggested in the current SAS analysis threads and *XMM-Newton* Users Handbook.¹² We generated count rate histograms for all observations with energies above 10 keV to determine the time intervals where the emission from the MOS cameras was affected by periods of high background and/or photon flares. The effective exposures of the MOS1 and MOS2 observations after filtering are shown in Table 2.

¹¹ Documentation related to the SAS package, as well as its download, is distributed by XMM-Newton Science Operations Center at <http://xmm.esac.esa.int/sas/>.

¹² http://xmm.esac.esa.int/external/xmm_user_support/documentation/uhb/index.html

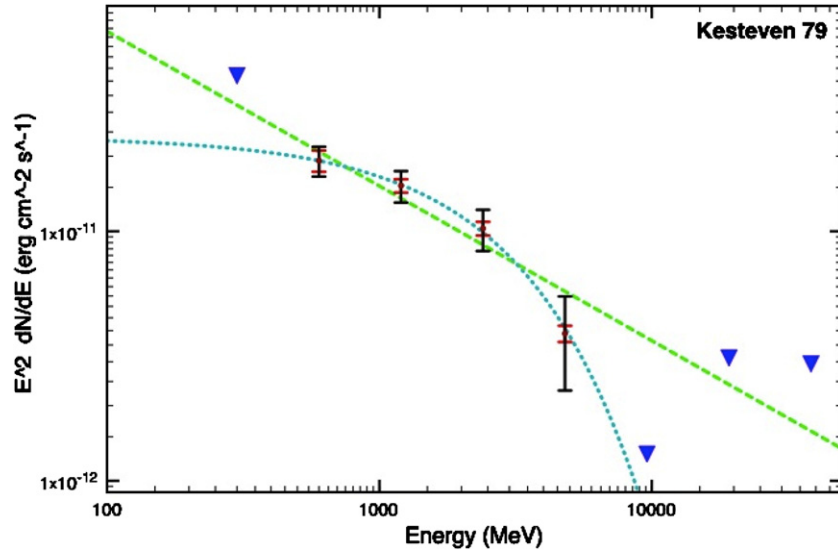


Figure 2. *Fermi*-LAT gamma-ray spectrum of Kesteven 79. The statistical errors are plotted in black, systematic errors are plotted in red, and upper limits are plotted in blue. The simple power law models and exponential cut-off model described by the parameters in Table 1 are shown as the green dotted line and the cyan dashed line, respectively.

(A color version of this figure is available in the online journal.)

Table 1
The Spatial and Spectral Fit Parameters for the Kes 79 *Fermi*-LAT Data

Name	Spatial			Spectral Fit					TS Value
	R.A. (deg)	Decl. (deg)	$F(0.1\text{--}100\text{ GeV})$ (10^{-7} photons $\text{GeV cm}^{-2} \text{s}^{-1}$)	Γ_{pwl}	χ^2_{pwl} (dof)	Γ_{cut}	E_{cut} (GeV)	χ^2_{exp} (dof)	
Kes 79	283.121	+0.645	$0.63^{+0.70}_{-0.30}$	2.62 ± 0.12	2.87(2)	2.00 ± 0.38	2.71 ± 0.64	0.27(1)	$\sim 7\sigma$

Table 2
Archival *XMM-Newton* Observations of Kes 79 and Their Corresponding Total and Effective Exposure Times as Used in Our Analysis

Obs. ID	R.A. (J2000)	Decl. (J2000)	Observation Date	Exposure (ks)	MOS 1	MOS 2
					Good Exposure (ks)	Good Exposure (ks)
204970201	18 52 35.54	+00 39 40.4	2010 Apr 18	31.4	28.7	30.3
204970301	18 52 35.65	+00 39 36.4	2010 Apr 23	31.4	30.9	30.5
400390201	18 52 34.90	+00 39 42.4	2010 Jun 8	30.4	28.7	29.4
400390301	18 52 42.56	+00 40 52.2	2003 Jul 20	34.5	34	33.6
550670201	18 52 34.72	+00 39 48.7	2009 Aug 19	26.9	21.6	21.8
550670301	18 52 34.61	+00 39 46.3	2009 Aug 21	35.4	30.4	30.5
550670401	18 52 34.64	+00 39 48.1	2009 Aug 23	40.4	36.1	35.5
550670501	18 52 34.68	+00 39 43.0	2009 Aug 29	34.1	32.7	33.1
550670601	18 52 34.82	+00 39 43.7	2010 Aug 10	40.4	34.7	34.1
550670901	18 52 42.67	+00 40 48.5	2003 Sep 17	26.9	25	25.4
550671001	18 52 42.53	+00 40 49.0	2003 Sep 16	27.9	23.5	24.5
550671101	18 52 42.31	+00 40 50.4	2003 Sep 25	23.0	19.0	18.7
550671201	18 52 42.49	+00 40 52.2	2003 Sep 23	27.9	17.7	19.4
550671301	18 52 42.24	+00 40 58.1	2004 Sep 4	26.9	22.2	22.7
550671401	18 52 42.67	+00 40 48.4	2003 Sep 17	5.93	5.4	5.3
550671501	18 52 42.28	+00 40 52.0	2003 Sep 25	6.42	0.0	4.3
550671601	18 52 42.49	+00 40 52.0	2003 Sep 23	5.63	5.0	5.1
550671701	18 52 42.24	+00 40 57.9	2004 Sep 4	4.43	3.7	3.8
550671801	18 52 41.92	+00 41 02.9	2004 Sep 22	28.9	25.4	25
550671901	18 52 42.10	+00 40 58.4	2004 Sep 10	31.4	18.1	19.5
550672001	18 52 42.10	+00 40 58.3	2004 Sep 10	5.13	3.8	3.6

3.1. Imaging

To analyze the morphology of Kes 79, we produced an image of the entire remnant by combining all 21 filtered observations of MOS1 and MOS2 using the SAS task *emosaic*. This task

produces a single exposure-corrected intensity image of the SNR. For each camera, we generated maps in the energy bands 0.5–1.195 keV, 1.195–1.99 keV, and 1.99–7.00 keV.

The *XMM-Newton* EPIC MOS mosaic image of Kes 79 in the 0.5–7.0 keV band is presented in Figure 3(a). The

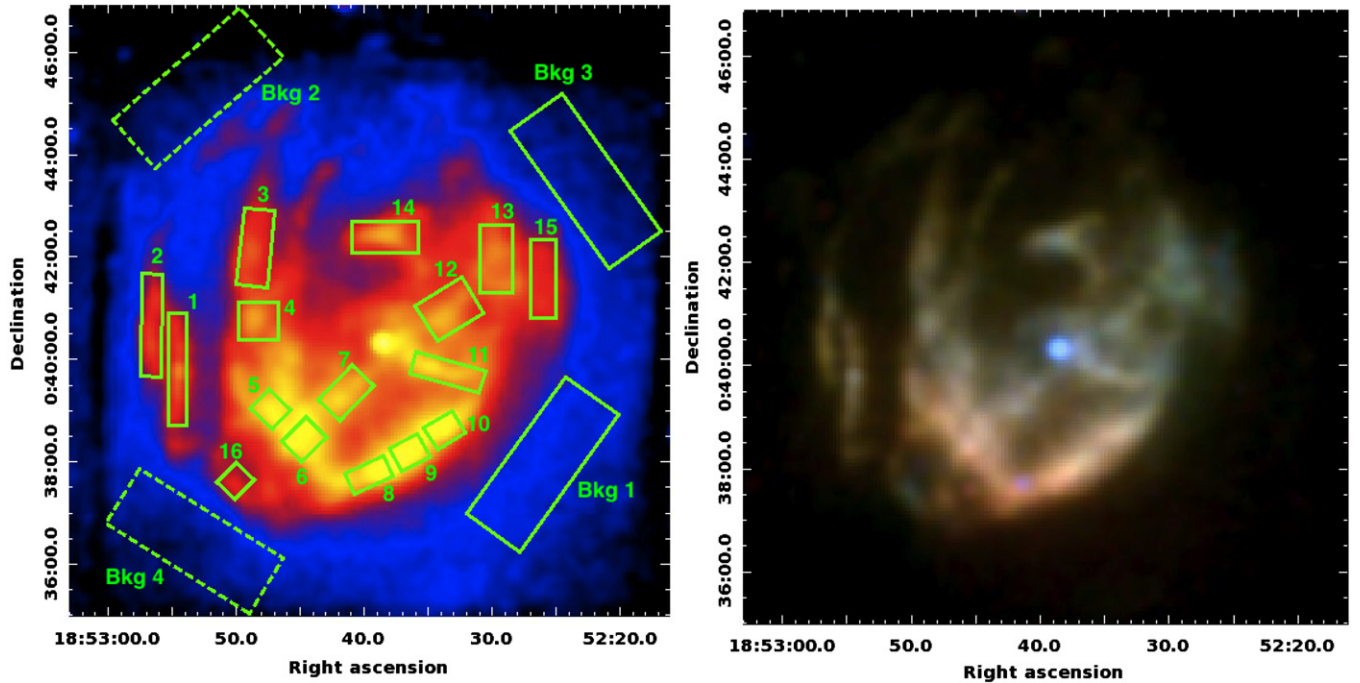


Figure 3. (a) A 0.5–7 keV exposure corrected image of the X-ray emission from Kes 79. This was created using the *XMM-Newton* SAS task *emosaic*. The image has been smoothed with a Gaussian function of width $3''$. Overlaid in green are the regions we use for spectral extraction, described in Section 3.2, and the four background regions we used. (b) Exposure corrected RGB image of SNR Kes 79 created using EPIC MOS1 and MOS2 data. Red corresponds to the 0.5–1.195 keV energy band, green to 1.195–1.99 keV, and blue to 1.99–7.00 keV. The RGB image has been smoothed with a Gaussian function of width $3''$. The relative intensity levels of the different color images have been adjusted to highlight spectral structures of the emission.

(A color version of this figure is available in the online journal.)

X-ray emission observed with *XMM-Newton* corresponds well to the rich spatial structure observed by Sun et al. (2004) using 29.3 ks of *Chandra* data. A large majority of the emission comes from the center of the remnant, with faint X-ray emission found toward the northeast. There are multiple faint and bright X-ray filaments and evidence of multiple partial shells highlighted by bright X-ray emission toward the south. Also observable in this image is the X-ray emission from the pulsar PSR J1852+0040. Our mosaic image mimics the 0.5–5 keV *XMM* image of Kes 79 by Giacani et al. (2009).

With the aim of analyzing any possible spectral variation in Kes 79, we also created an RGB image of the remnant, which is found in Figure 3(b). We generated this image by combining images of events from the MOS1 and MOS2 cameras in the energy bands 0.5–1.195 keV (red), 1.195–1.99 keV (green), and 1.99–7.00 keV (blue). The relative intensities of the color images have been adjusted in the RGB representation to highlight all structures. This image reveals a very filamentary and clumpy morphology, with the southern shell producing a significant amount of soft X-rays. The pulsar, which has a hard spectrum, is seen as the bright blue dot in the center of the image.

3.2. Spectroscopy

The aim of our spectral analysis of Kes 79 is to perform a spatially resolved spectral study of the remnant. To do this, we analyze the variation in the spectral parameters in different regions of the remnant.

For our analysis, we used *XMM* observations that had a good exposure time of 10 ks or more, as the event files with less than this amount produced spectra with less than 100 counts. The X-ray spectra were extracted from the filtered and cleaned event files using the SAS task *evselect*. The tasks *arfgen* and *rmfgen*

were used to generate a spectral response and effective area file for each extracted region.

The background of *XMM-Newton* consists of the Cosmic X-ray background and a time-variable non-X-ray background resulting from electronic noise, solar protons, and CRs interacting with the detector (Kuntz & Snowden 2008). Above ~ 5 keV, the X-ray spectrum for these observations is dominated by background. We accounted for the background of each observation by selecting four source-free regions as shown in Figure 3(a). Four background regions were selected to ensure that any gaps due to mosaicking would not affect the spectra obtained.

The combined spectra were analyzed with the X-ray software XSPEC version 12.8.0, over an energy range of 0.5–10 keV. Each energy bin was required to have a minimum of 25 counts and the reduced χ^2 statistic was used as the best-fit model discriminator. To investigate the emission of the remnant, we used the non-equilibrium ionization (NEI) plasma emission models, PSHOCK and VPSHOCK (Borkowski et al. 2001). These models describe a plane-parallel shock front interacting with a plasma and are characterized by a constant electron temperature (kT) and an upper and lower limit on the ionization timescale ($\tau_l = n_e t_l$ and $\tau_u = n_e t_u$). The absorption, upper limit of the ionization timescale, temperature, normalization of both models, and the abundances of Ne, Mg, Si, and S, were left as free parameters. All other elemental abundances were frozen to the solar values of Wilms et al. (2000) once we verified that their variation did not significantly improve the model fit of the data. As these NEI models do not include atomic data for the Argon emission, an additional Gaussian component with a width of 0.01 keV and line energy of 3.1396 keV was added to account for this feature in the spectra fitting. The normalization of this additional component was left free.

3.2.1. Spectral Properties of Individual Regions

To investigate the spectral variation across Kes 79, we perform a spatially resolved spectral analysis by extracting X-ray spectra from 16 regions shown in green in Figure 3(a). These regions were selected as they correspond to variations in the color distribution in the RGB image or variation in the flux as observed in the X-ray image. To increase the signal-to-noise ratio, we combined the X-ray spectra extracted for all 16 MOS1 and MOS2 observations with good time events of 10 ks or greater, producing combined MOS1 and combined MOS2 X-ray spectra for each region. This was done by using the HEASOFT tasks *mathpha*, *fparkey*, *marfmr*, and *addrmf*. The combined spectra for all regions were grouped using the FTOOLS command *grppha*.

Initially, the spectra from all extracted regions were fitted using a single component model (VPSHOCK) and the XSPEC absorption model TBABS (Wilms et al. 2000). By itself, TBABS*VPSHOCK was able to account reasonably well for the X-ray emission below ~ 3 keV, but it failed to fit the higher energy component of the spectrum, and as a consequence the fits resulted in relatively large reduced chi-squared values ($\chi^2/\text{dof} > 1.80$). Subsequently, we fitted the spectra of each region with a two-component plasma model, VPSHOCK+PSHOCK, and TBABS. The parameters of the best-fit models for all extracted spectra are shown in Table 3, where the uncertainties correspond to the 90% confidence level.

All regions require two thermal components, indicating that the plasma of Kes 79 contains a soft and hard temperature component. The temperatures derived for the hard component in regions 3–14 range between 0.61 ± 0.03 and 1.36 ± 0.3 keV, while for the filamentary structures encompassed by regions 1–2, the hard temperatures are equal to $0.55^{+0.03}_{-0.01}$ keV and 0.49 ± 0.03 keV, respectively. The derived VPSHOCK temperatures for regions 3–14 are, on average, comparable to the temperature derived by Sun et al. (2004) and Giacani et al. (2009), who used a single component NEI model, while the temperature of the filamentary structures are lower than global temperatures derived by Sun et al. (2004) and Giacani et al. (2009). The soft plasma (PSHOCK) component of Kes 79's X-ray emitting material is highly isothermal in nature, with all regions requiring a temperature of ~ 0.24 keV.

All region-specific spectra are similar to each other, with strong emission lines coming from Si, S, and Mg, with some requiring Ne and Ar. All regions in the high kT component have super-solar abundances (e.g., larger than ~ 2 times solar abundance) of Si and S, while Mg has ~ 1.5 times solar abundance. We thus associate this component with shocked ejecta. All regions require approximately solar abundances of Ne, with the exception of region 7, which has an enhancement of Ne. Region 15 has the largest elemental abundances out of all the regions analyzed, with Mg, Si, and S requiring super-solar abundances. The inner regions closest to the X-ray position of the pulsar (regions 7, 11, and 12), and the filament described by region 2, all require the highest abundances of Mg, Si, and S overall. All regions require enhanced abundances of Mg, Si, and S, which indicates that the ejecta component is found everywhere throughout the remnant, implying that we observed X-ray emission from shocked ejecta. The abundances obtained in this analysis are larger than the values obtained by Sun et al. (2004) using their ionization equilibrium collisional plasma model or NEI collisional plasma models. This arises from the fact that in our analysis, we use the abundance table by Wilms et al. (2000), while Sun et al. (2004) uses the table derived by Anders & Grevesse (1989).

The shocked ejecta, modeled using VPSHOCK, have an ionization timescale of $\sim 10^{11} \text{ cm}^{-3} \text{ s}$ in all regions. These values agree well with the ionization timescales derived by Sun et al. (2004) and Giacani et al. (2009). The ionization timescale of the material swept up by the forward shock as derived using the PSHOCK model is fixed to $1 \times 10^{12} \text{ cm}^{-3} \text{ s}$, as initial spectral analysis yielded ionization timescales of this magnitude. The high ionization timescale of all regions indicates that the soft plasma component is in ionization equilibrium (Vink 2012), while the hard plasma component across the whole remnant is far from ionization equilibrium.

The derived hydrogen column density for each region ranges between $(2.08^{+0.03}_{-0.04} - 2.75^{+0.03}_{-0.04}) \times 10^{22} \text{ cm}^2$. These values are higher than the estimated absorbing column density derived by Sun et al. (2004) using *Chandra* data ($\sim 1.6 \times 10^{22} \text{ cm}^2$) and Giacani et al. (2009) using *XMM-Newton* data ($\sim 1.5 \times 10^{22} \text{ cm}^2$). This discrepancy most likely arises from the fact that we use a different abundance table in our analysis and a two-component plasma model. These derived values indicate that the X-ray spectrum of Kes 79 is heavily absorbed by interstellar material.

3.2.2. Global Spectral Properties

To investigate the average spectral properties of Kes 79, we extracted a global X-ray spectrum from a circular region centered at $(\alpha_{J2000}, \delta_{J2000}) = (18^{\text{h}}52^{\text{m}}41^{\text{s}}.31, +0^{\circ}40'52''.97)$ with a radius of 4.70 arcmin. This region enclosed the complete SNR as observed in X-rays. The background spectrum was extracted using the four source-free regions shown in Figure 3(a). We did this for each observation with good exposure times of 10 ks or greater and all spectra are binned with a minimum of 25 counts. We fit all 16 MOS1 and MOS2 observations simultaneously over an energy range of 0.5–10 keV. Similar to the spatial X-ray analysis, a single-component VPSHOCK model with enhanced abundances of Si, S, and Mg produced unsatisfactory fits, and was improved when we added a thermal component (PSHOCK) ($\chi^2/\text{dof} = 1.07$). Figure 4 shows the global X-ray spectrum of Kes 79, while the values of these best-fit parameters with their corresponding 1σ uncertainties are found in Table 4. This result implies that the plasma of Kes 79 consists of a hard component with a plasma temperature of $0.77^{+0.006}_{-0.001}$ keV and a soft component with a temperature of $0.24^{+0.0002}_{-0.001}$ keV. This is consistent with our fits of the individual regions. The temperatures derived by Sun et al. (2004) and Giacani et al. (2009) using *Chandra* and *XMM* data is similar to the temperature of the hard plasma component. The best-fit absorbing column density is $N_{\text{H}} = 2.35^{+0.003}_{-0.001} \times 10^{22} \text{ cm}^2$ and is higher than values obtained by Sun et al. (2004) and Giacani et al. (2009) using a single NEI plasma model. Using the Anders and Grevesse abundance table, we obtained a column density similar to that obtained by Sun et al. (2004) and Giacani et al. (2009).

Using the best fit of the global X-ray spectrum and the total count rate, we derive an unabsorbed flux, for an energy range of 0.5–10 keV, of $9.8 \times 10^{-10} \text{ erg cm}^{-2} \text{ s}^{-1}$ and a luminosity of $5.6 \times 10^{36} \text{ erg s}^{-1}$ assuming a distance of 7 kpc. The luminosity derived in this analysis is a factor of two larger than the flux obtained by Sun et al. (2004) using *Chandra* and this most likely arises from the fact that we use a two component NEI plasma model, while Sun et al. (2004) uses a one component NEI model for their analysis.

3.2.3. X-ray Characteristics of Kes 79

Using the PSHOCK+VPSHOCK model parameters summarized in Table 3, we derive the density of the X-ray emitting

Table 3

Results from Fitting the Two-component Model, the VPSHOCK+PSHOCK Model, and the XSPEC Absorption Model TBABS to the 16 Different Regions Defined in Figure 3(a) with the 90% Confidence Ranges

Region	TBABS	Soft Component (PSHOCK)			Hard Component (VPSHOCK)							$\chi^2/(\text{dof})$
	nH (10^{22} cm^2)	kT (keV)	τ_u ($10^{12} \text{ s cm}^{-3}$)	Norm cm^{-5} (10^{-2})	kT (keV)	τ ($10^{11} \text{ s cm}^{-3}$)	Norm cm^{-5} (10^{-3})	Ne	Mg	Si	S	
1	2.43 ± 0.05	0.19 ± 0.01	1	$5.94^{+2.5}_{-2.0}$	$0.55^{+0.03}_{-0.01}$	$2.76^{+0.6}_{-0.7}$	$3.61^{+0.1}_{-0.5}$...	1.29 ± 0.8	$2.31^{+0.1}_{-0.2}$	2.50 ± 0.3	1.19
2	$2.51^{+0.06}_{-0.03}$	0.20 ± 0.02	1	$3.14^{+2.5}_{-1.3}$	0.49 ± 0.03	$2.61^{+0.9}_{-0.6}$	$3.41^{+1.0}_{-1.1}$...	1.42 ± 0.1	2.69 ± 0.3	$2.83^{+0.5}_{-0.4}$	1.10
3	$2.48^{+0.04}_{-0.02}$	0.25 ± 0.01	1	$3.77^{+1.2}_{-0.3}$	$0.78^{+0.02}_{-0.04}$	1.56 ± 0.2	$2.71^{+0.6}_{-0.2}$...	$1.52^{+0.08}_{-0.1}$	$2.53^{+0.2}_{-0.1}$	2.53 ± 0.2	1.24
4	$2.14^{+0.02}_{-0.03}$	0.22 ± 0.01	1	$3.62^{+0.3}_{-0.4}$	$0.69^{+0.01}_{-0.02}$	$1.99^{+0.3}_{-0.1}$	$3.51^{+0.4}_{-0.2}$...	$1.44^{+0.06}_{-0.05}$	$2.18^{+0.09}_{-0.06}$	2.33 ± 0.12	1.32
5	$2.12^{+0.02}_{-0.01}$	0.23 ± 0.005	1	$4.00^{+1.2}_{-0.6}$	0.75 ± 0.02	1.74 ± 0.2	3.89 ± 0.3	...	$1.39^{+0.05}_{-0.04}$	$2.11^{+0.06}_{-0.05}$	2.06 ± 0.1	1.34
6	2.27 ± 0.03	$0.25^{+0.009}_{-0.003}$	1	$3.72^{+0.7}_{-0.4}$	$0.80^{+0.03}_{-0.01}$	$2.44^{+0.2}_{-0.3}$	$4.40^{+0.09}_{-0.64}$...	1.40 ± 0.04	1.94 ± 0.06	$1.88^{+0.12}_{-0.08}$	1.35
7	$2.08^{+0.03}_{-0.04}$	0.26 ± 0.01	1	$3.67^{+0.4}_{-0.6}$	$1.05^{+0.05}_{-0.09}$	$9.25^{+0.16}_{-0.07}$	$1.34^{+0.6}_{-0.2}$	1.79 ± 0.27	$1.84^{+0.13}_{-0.19}$	$3.23^{+0.44}_{-0.48}$	$2.87^{+0.30}_{-0.46}$	1.43
8	$2.09^{+0.02}_{-0.04}$	$0.25^{+0.02}_{-0.01}$	1	$2.35^{+0.4}_{-0.6}$	$0.67^{+0.03}_{-0.02}$	$3.31^{+0.6}_{-0.5}$	$4.08^{+0.6}_{-0.4}$...	$1.41^{+0.07}_{-0.05}$	2.07 ± 0.1	2.25 ± 0.2	1.38
9	2.30 ± 0.03	0.23 ± 0.01	1	4.09 ± 0.1	$0.73^{+0.04}_{-0.02}$	$2.34^{+0.2}_{-0.3}$	$3.15^{+0.3}_{-0.6}$	$1.28^{+0.3}_{-0.1}$	$1.56^{+0.2}_{-0.1}$	$2.35^{+0.3}_{-0.1}$	$2.33^{+0.3}_{-0.1}$	1.36
10	$2.61^{+0.02}_{-0.04}$	$0.26^{+0.003}_{-0.005}$	1	$5.74^{+0.3}_{-0.2}$	0.90 ± 0.2	1.57 ± 0.10	$4.54^{+0.3}_{-0.2}$	0.94 ± 0.1	$1.28^{+0.06}_{-0.07}$	$2.03^{+0.09}_{-0.08}$	1.97 ± 0.1	1.34
11	$2.62^{+0.03}_{-0.02}$	$0.25^{+0.003}_{-0.004}$	1	$7.78^{+0.7}_{-2.2}$	$0.80^{+0.01}_{-0.03}$	1.59 ± 0.1	$5.14^{+0.7}_{-0.6}$	$1.18^{+0.1}_{-0.2}$	$1.70^{+0.05}_{-0.06}$	2.72 ± 0.2	2.42 ± 0.1	1.34
12	$2.75^{+0.03}_{-0.04}$	0.23 ± 0.01	1	$8.65^{+3.0}_{-1.8}$	$0.81^{+0.03}_{-0.05}$	$0.96^{+0.06}_{-0.05}$	$3.12^{+0.6}_{-0.5}$...	$2.09^{+0.1}_{-0.2}$	$4.39^{+0.2}_{-0.4}$	$3.63^{+0.3}_{-0.2}$	1.53
13	$2.50^{+0.06}_{-0.04}$	0.23 ± 0.02	1	$3.03^{+1.6}_{-0.7}$	0.61 ± 0.03	$3.66^{+0.7}_{-1.1}$	4.71 ± 0.8	$0.84^{+0.2}_{-0.1}$	1.34 ± 0.06	$2.01^{+0.2}_{-0.1}$	$2.17^{+0.2}_{-0.1}$	1.18
14	$2.53^{+0.04}_{-0.07}$	0.23 ± 0.02	1	3.49 ± 1.2	$0.65^{+0.03}_{-0.04}$	2.92 ± 0.8	4.14 ± 0.9	0.91 ± 0.2	1.35 ± 0.1	2.04 ± 0.2	2.13 ± 0.2	1.22
15	2.45 ± 0.1	$0.22^{+0.03}_{-0.02}$	1	1.56 ± 0.1	1.36 ± 0.3	0.41 ± 0.09	0.17 ± 0.01	...	$2.38^{+0.5}_{-0.6}$	$5.81^{+2.3}_{-1.7}$	$4.14^{+1.6}_{-1.1}$	1.09
16	$2.51^{+0.05}_{-0.06}$	0.24 ± 0.02	1	$3.08^{+1.6}_{-1.0}$	0.62 ± 0.03	$3.60^{+1.4}_{-0.9}$	$4.65^{+0.9}_{-0.5}$	0.56 ± 0.2	$1.34^{+0.09}_{-0.08}$	$2.04^{+0.3}_{-0.2}$	2.21 ± 0.2	1.18

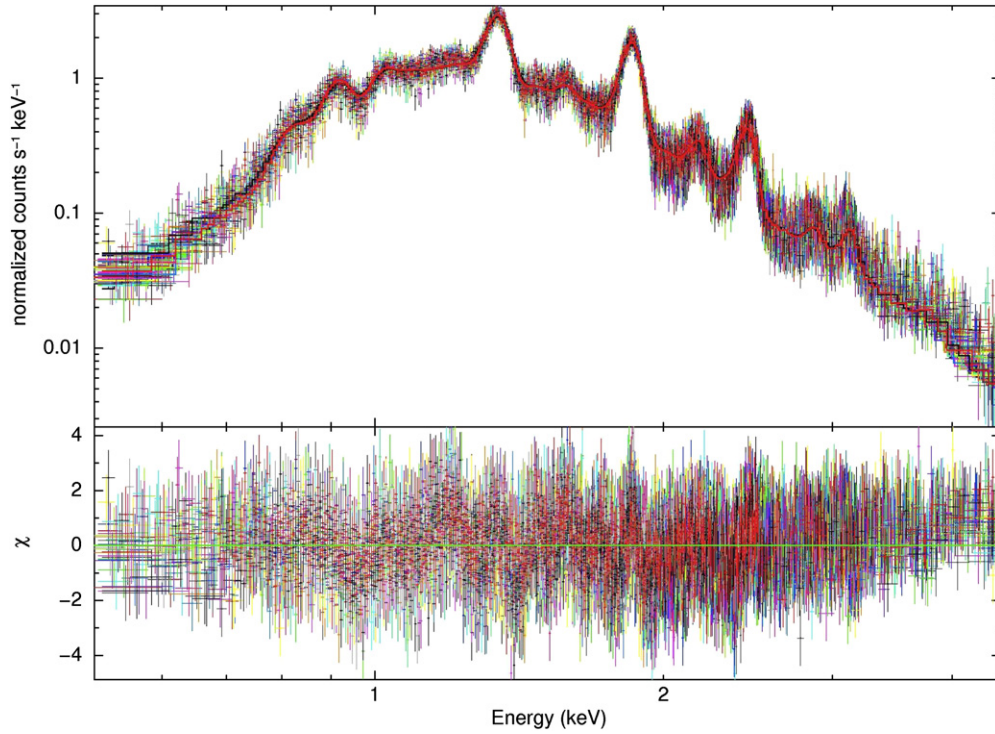


Figure 4. MOS1 and MOS2 spectrum extracted from 16 *XMM-Newton* observations with good time intervals of 10 ks or more for the whole of Kes 79. These spectra have been fitted simultaneously with a two-component plasma model, VPSHOCK+PSHOCK, and the XSPEC absorption model TBABS described by the parameters in Table 4. The X-ray spectra are overlaid with the fitted VPSHOCK+PSHOCK model and their chi-square residuals are shown. The combined MOS1 and MOS2 X-ray spectra derived for each region shown in Figure 3(a) all have features similar to the global X-ray spectrum shown here.

(A color version of this figure is available in the online journal.)

Table 4

Results from Fitting the Two-component Model and the VPSHOCK+PSHOCK Model to the Whole SNR with 90% Confidence Ranges

Parameters	Global Fit
n_H (10^{22} cm^{-2})	$2.35^{+0.003}_{-0.01}$
<i>Soft component (PSHOCK)</i>	
kT (keV)	$0.24^{+0.0002}_{-0.001}$
τ ($10^{12} \text{ s cm}^{-3}$)	1
Norm (cm^{-5})	$0.67^{+0.0002}_{-0.001}$
Absorbed flux for 0.5–10 keV ($\text{erg cm}^{-2} \text{ s}^{-1}$)	2.65×10^{-12}
Unabsorbed flux for 0.5–10 keV ($\text{erg cm}^{-2} \text{ s}^{-1}$)	7.68×10^{-10}
<i>Hard component (VPSHOCK)</i>	
kT (eV)	$0.78^{+0.006}_{-0.001}$
τ ($10^{11} \text{ s cm}^{-3}$)	1.57 ± 0.03
Norm cm^{-5}	$0.06^{+0.01}_{-0.02}$
Mg	$1.41^{+0.02}_{-0.01}$
Si	2.33 ± 0.02
S	2.28 ± 0.03
Absorbed flux for 0.5–10 keV ($\text{erg cm}^{-2} \text{ s}^{-1}$)	$7.90 \times 10^{-12} \text{ erg cm}^{-2} \text{ s}^{-1}$
Unabsorbed flux for 0.5–10 keV ($\text{erg cm}^{-2} \text{ s}^{-1}$)	$2.09 \times 10^{-10} \text{ erg cm}^{-2} \text{ s}^{-1}$
$\chi^2/(\text{dof})$	1.07
Total luminosity (0.5–10 keV)	$5.6 \times 10^{36} \text{ erg s}^{-1}$

material and how it changes across the remnant. In our calculations, we set the radius (R) of Kes 79 to 4.7 arcmin, which corresponds to a physical size of $9.6 d_7$ pc. For each individual region, the X-ray emitting volume was estimated by taking an area equivalent to the extracted SNR regions (Figure 3(a)) and projecting this area through a shell (front and back) with a thickness of $R/12$. The volume emission measure (EM), which de-

scribes the amount of plasma available to produce the observed X-ray flux, is defined as $EM \sim \int n_e n_H dV_X \sim n_e n_H f V_X$, where n_e is the post-shock electron density, n_H is the mean hydrogen density, and f is a volume filling factor. The EM is estimated using the normalization of the X-ray spectral fits using $K = (10^{-14}/4\pi d^2)EM$. Assuming a strong shock, the ambient density can be calculated using $n_0^2 = (K d^2 \pi)/(4.8 \times 10^{-14} f V_X)$. From this, we can calculate the ambient density (n_0) across the remnant (i.e., for each region). These n_0 calculations are summarized in Table 5. The inferred ambient density across the remnant ranges from $n_0 = (1.81 \pm 0.5 - 4.85^{+1.1}_{-0.9}) f^{-1/2} d_7^{-1/2} \text{ cm}^{-3}$. These high ambient density values indicate that the remnant is expanding into a dense environment. The ambient density is highest in regions 5, 6, 9, 10, 11, and 16, which are predominantly toward the south and southeast of the remnant. This observation is consistent with the presence of a nearby MC overlapping the eastern and southeastern regions of Kes 79. The presence of X-ray emission in these regions may imply the interaction of the remnant's shock-wave with the MC.

Our estimates of the ambient density are an order of magnitude larger than the estimated ambient density by Sun et al. (2004). This results from the higher column density derived using the Wilms et al. (2000) abundance table. This absorption hides a significant soft component, which comprises a large total mass and results in a high derived density. The temperature derived by Sun et al. (2004) using the three non-ionization equilibrium models in their paper have approximately intermediate values of the soft and hard temperature components derived from our spatial dependent and global X-ray spectra (Tables 3 and 4, respectively). This could imply that the short *Chandra* observation could not distinguish between the two plasma components suggested by our extracted X-ray spectra and instead

Table 5
Derived Ambient Density Estimates for the 16 Different
Regions Shown in Figure 3(a)

Region	Ambient Density ($d_7 f^{-0.5} \text{ cm}^{-3}$)
1	$3.39^{+2.2}_{-2.0}$
2	$2.52^{+2.2}_{-1.6}$
3	$2.49^{+1.4}_{-0.6}$
4	$3.15^{+0.9}_{-1.0}$
5	$4.29^{+2.3}_{-1.7}$
6	$3.59^{+1.6}_{-1.2}$
7	$3.08^{+1.0}_{-1.2}$
8	$2.68^{+1.1}_{-1.4}$
9	3.95 ± 0.6
10	$4.85^{+1.1}_{-0.9}$
11	$4.29^{+1.3}_{-2.3}$
12	$3.94^{+2.3}_{-1.8}$
13	$2.34^{+1.7}_{-1.1}$
14	2.55 ± 1.5
15	1.81 ± 0.5
16	$3.51^{+2.5}_{-2.0}$

Notes. These values are calculated from the best-fit parameters of our two component plasma models, VPSHOCK+PSHOCK, and the XSPEC absorption model TBABS shown in Table 3.

represents an average of the soft and hard components summed along the line of sight.

In the Sedov phase of evolution, the SNR radius scales as $R \propto n_0^{-1/5}$, at a given age. Thus, while our analysis indicates a somewhat non-uniform ambient medium, the overall behavior can be reasonably approximated by assuming evolution in a uniform medium (Hnatyk & Petruk 1999). When calculating the global characteristics of Kes 79, we estimate the volume of the X-ray emitting region (V_X) by assuming that the plasma fills a spherical shell with a radius of 9.6 d_7 pc, a thickness of two times $R/12$ and the X-ray parameters listed in Table 4. The shock temperature can be derived by using $T_{\text{sh}} = 0.79T_X$, where T_X is the temperature inferred from the X-ray fit, assuming electron-ion temperature equilibrium. Using the global temperature for the soft component (PSHOCK) which is suggested to be the forward shock component, we obtain a shock temperature of $T_{\text{sh}} \sim 0.19$ keV. The forward shock velocity is determined using $v_{\text{sh}} = [(16kT_{\text{sh}})/(3\mu m_H)]^{1/2}$, where $\mu = 0.604$ is the mean atomic weight, k is Boltzmann's constant and m_H is the mass of hydrogen. We obtain a shock velocity of $v_{\text{sh}} \sim 400 \text{ km s}^{-1}$, assuming electron-ion temperature equilibrium. The Sedov age of the remnant is related to the forward shock velocity by $t_{\text{SNR}} = 2r_{\text{sh}}/5v_{\text{sh}}$. Assuming the SNR radius of $r_{\text{sh}} = 4.7$ arcmin, we derive an age of $\sim 9400d_7$ yr. Our spatial X-ray analysis described by the model parameters in Table 3 gives a t_{age} between ~ 9000 – 10600 yr whose average is approximately the t_{age} that we derived in the global analysis. Sun et al. (2004), using different X-ray model parameters, derived an age of Kes 79 of 5400–7500 yr, while Giacani et al. (2009), using VLA radio data, derived an upper limit of $t_{\text{age}} < 15 \times 10^3$ yr. The explosion energy is calculated using $E_{\text{SNR}} = 0.7r_{\text{sh}}^5 m_p n_0 t_{\text{SNR}}^{-2}$ and we obtain $E_{\text{SNR}} \sim 3.7 \times 10^{50} f^{-1/2} d_7^{-5/2}$ erg. This value is lower than the canonical 10^{51} erg. This low value for the explo-

sion energy has been inferred from X-ray observations of a number of other SNRs, e.g., G272.2–3.2 (Harrus et al. 2001) and G299.2–2.9 (Park et al. 2007). Castro et al. (2011), suggested that such low inferred explosion energies could be a signature of efficient CR acceleration during the evolution of the SNR, consistent with the detection of γ -rays from Kes 79 (see below). The X-ray emitting mass is calculated using $M_X = 1.4n_H m_H f V$ and we obtain $M_X \sim 160 f^{1/2} d_{7.1}^{5/2} M_\odot$ of swept-up ISM.

4. DISCUSSION

Non-thermal X-ray and γ -ray emission from SNRs indicate that a population of particles are being accelerated to VHEs by the SNR shock front. γ -rays can be produced by leptonic mechanisms such as inverse Compton scattering, non-thermal bremsstrahlung, or by hadronic mechanisms via the decay of neutral pions generated during proton-proton interactions. SNR shocks are not the only astrophysical sources capable of producing γ -rays. Pulsars can also contribute to the observed γ -ray emission and their contribution should also be considered before we assume that the γ -ray sources are products of particles being accelerated at the SNR shock.

4.1. Pulsar Contribution to γ -rays

In the first *Fermi*-LAT Pulsar catalog, Abdo et al. (2010c) determined that the spectra of pulsars detected in the *Fermi*-LAT energy band are best described by a power-law distribution with an exponential cut-off of 1–5 GeV, with the exception of the Crab pulsar, which can be described using an exponential cut-off of >100 GeV (Aliu et al. 2011). This result was confirmed and presented in the second *Fermi*-LAT Pulsar catalog (Abdo et al. 2013) in which the *Fermi*-LAT collaboration analyzed three years of *Fermi*-LAT data and detected with high confidence 117 γ -ray pulsars above an energy of 0.1 GeV. Most recently, a preliminary analysis of pulsars detected by the *Fermi*-LAT satellite by Saz Parkinson & *Fermi*-LAT Collaboration (2012) indicated that a number of pulsars show possible evidence of high-energy emission with a cut-off energy >10 GeV. The spectra of the source coincident with Kes 79 can be best fit using an exponential cut-off of $E_{\text{cut}} \sim 2.62$ GeV and $E_{\text{cut}} \sim 1.5$ GeV, respectively, which falls within the expected range for E_{cut} for γ -ray pulsars. As a consequence, the hypothesis that the observed γ -ray emission could be due to the presence of a pulsar cannot be ruled out straight away.

Within a 5° region centered on the observed γ -ray emission of Kes 79 (Figure 1(a)), there are three pulsars in the Australian Telescope National Facility (ATNF) Pulsar Catalogue (Manchester et al. 2005),¹³ whose spin down power is sufficient to produce the γ -ray flux of Kes 79 if, at the distance of the pulsar, all of that power goes into γ -rays. An upper limit on the γ -ray flux of each ATNF pulsar is calculated by using the distance to the pulsar listed in the catalog, and by assuming that 100% of the spin down power, \dot{E} , is converted into γ -rays. The upper limit on the pulsar's γ -ray flux is comparable to the observed γ -ray flux of Kes 79. This indicates that these three pulsars could potentially contribute to the observed γ -rays. The pulsars would also have to be located such that the *Fermi*-LAT's PSF could not resolve them as separate sources. At 0.6 GeV, which corresponds to the energy of the first data point of Kes 79's γ -ray spectrum, the resolution of the PSF of the *Fermi*-LAT is

¹³ The ATNF Catalogue contains the positional and physical characteristics of 1509 pulsars, which can be found at <http://www.atnf.csiro.au/research/pulsar/psrcat>.

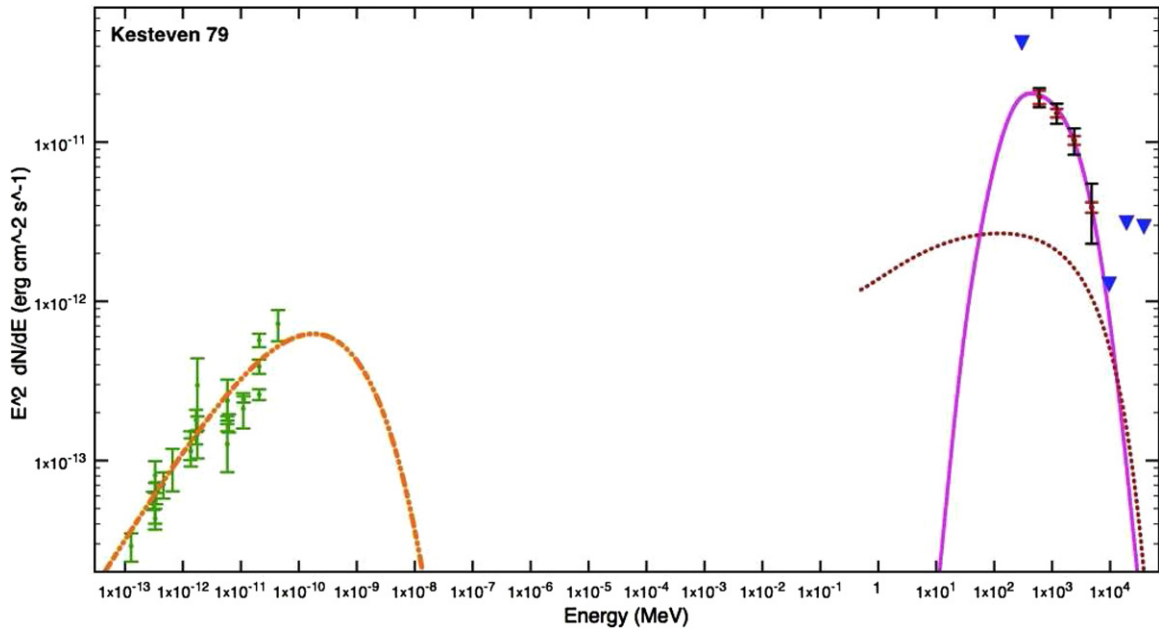


Figure 5. Broadband fits to radio (green data points) and *Fermi*-LAT γ -ray data points (as described in Figure 2) of Kes 79. The pion decay, non-thermal bremsstrahlung, and synchrotron models defined by the parameters in Table 6 are shown as the solid magenta line, dotted dark red line, and dot-dashed orange line, respectively. The corresponding IC model falls below the plotted axis.

(A color version of this figure is available in the online journal.)

$\sim 1^\circ$ for front events at 68% containment.¹⁴ All three pulsars are at a distance of 1.23° or more from the centroid of the γ -ray emission, thus making it highly unlikely that any of these pulsars are contributing significantly to the observed γ -ray emission of Kes 79. The 105 ms X-ray pulsar, PSR J1852+00040, discovered by Gotthelf et al. (2005) and Seward et al. (2003) to be associated with Kes 79, has a spin down power $\dot{E} = 3 \times 10^{32}$ erg s⁻¹ (Halpern & Gotthelf 2010). If all of this spin down energy is converted into γ -rays at the distance of the pulsar, it is incapable of producing the γ -ray flux we observe. Thus, we can state with confidence that this pulsar is not producing the observed γ -ray emission of Kes 79.

4.2. Hadronic Origin of γ -rays

As there is a lack of evidence in favor of significant γ -ray contribution from a pulsar, it is reasonable to assume that the observed γ -rays associated with Kes 79 arise from the SNR itself, a prospect made particularly likely by the high ambient density implied by our X-ray analysis in Section 3. This is supported by the presence of strong $\text{HCO}^+ J = 1 \rightarrow 0$ and $^{12}\text{CO} J = 1 \rightarrow 0$ emission found toward the east of the remnant and the fact that the remnant is thought to be interacting with dense molecular material (Scoville et al. 1987; Green 1989). In order to investigate the nature of the γ -ray emission, we first model the γ -ray spectrum, assuming that the γ -rays are produced predominantly by the decay of accelerated hadrons.

To reproduce the observed γ -ray spectrum of Kes 79, we use a model that simultaneously calculates the γ -ray emission, assuming a distribution of electrons and protons being accelerated at the SNR shock front. The π^0 decay model is based on a proton-proton interaction model by Kamae et al. (2006) with a scaling factor of 1.85 for helium and heavy nuclei (Mori 2009). The synchrotron and inverse Compton emission models are based on Baring et al. (1999) and the non-thermal

bremsstrahlung emission is modeled using the description in Bykov et al. (2000). To generate the momentum distribution of protons (or electrons) being accelerated by the SNR shock wave, we adopt a power law spectrum with an exponential cut-off, as expected from classical diffusive shock theory. This is described by

$$\frac{dN_i}{dp} = a_i p^{-a_i} \exp\left(-\frac{p}{p_{0i}}\right), \quad (1)$$

where i is the particle species, a_i is the normalization of the particle distribution, and p_{0i} is the exponential particle momentum cut-off. This particle distribution is transformed from momentum space to energy space, such that the exponential cut-off is defined by an input energy, E_{0i} . The integrals of each particle species distribution are summed and set such that the sum is equal to the assumed total energy in accelerated particles, $E_{\text{CR}} = \epsilon E_{\text{SN}}$, where ϵ is the efficiency of the SNR in depositing energy into CRs.

Figure 5 shows the model fits to the broadband emission observed from Kes 79. The radio spectrum of Kes 79, shown as the green data points in Figure 5(a), is a combination of multiple observations by Kundu & Velusamy (1967), Kesteven (1968), Beard & Kerr (1969), Altenhoff et al. (1970), Dulk & Slee (1972), Dickel (1973), Caswell et al. (1975, 1981), Becker & Kundu (1975), Dickel & Denoyer (1975), Slee (1977), Angerhofer et al. (1977), Kassim (1989, 1992), Kovalenko et al. (1994), and Giacani et al. (2009). We have plotted the pion decay model that adequately reproduces the observed γ -ray spectrum of Kes 79 as the solid magenta line, while the orange dot-dashed line corresponds to the synchrotron model which sufficiently reproduces the radio spectrum of each remnant, assuming an electron-positron ratio (K_{ep}) of 0.01. For completeness, we have also plotted the non-thermal bremsstrahlung contribution for Kes 79 as the dotted dark red line, while the corresponding IC model falls below the plotted axis. In Table 6, we have listed the parameters which reproduce the pion-decay, synchrotron, non-thermal bremsstrahlung and IC models observed in Figure 5.

¹⁴ http://www.slac.stanford.edu/exp/glast/groups/canda/lat_Performance.htm

Table 6
Model Parameters and Density Estimates for the Pion Decay Model for Kesteven 79

Object	Distance (kpc)	α_{proton}	α_{elec}	E_0^{proton} (GeV)	E_0^{elec} (GeV)	Magnetic Field (μG)	Ambient Density n_0 (cm^{-3})	X-Ray Density n_X (cm^{-3})	n_X Reference
Kes 79	7	4.09	3.8	12	12	180	14.5	$4_{-0.7}^{+0.9} d_7 f^{-0.5}$	Table 5

The γ -ray spectrum of Kes 79 is adequately described by a pion-decay model with a proton distribution that has a power law index of $\alpha_p = 4.09$ and a proton cut-off energy of $E_0^p \sim 12$ GeV. The cut-off energy for the proton spectrum required to model the γ -ray spectrum of Kes 79 under this hadronic-dominated scenario is rather low given that we expect cut-off energies for protons to be well in excess of a TeV (Reynolds 2008). This discrepancy could arise from efficient CR acceleration being suppressed in dense surrounding environments due to the suppression of Alfvén waves by ion-neutral collisions. This allows particles being accelerated by the SNR shock to escape the emission volume (Malkov et al. 2011, 2012).

To model the radio spectrum of Kes 79 using synchrotron emission, we assume that the cut-off energy of the electrons to be the same as the cut-off energy of the pion-decay model, as there is no non-thermal X-ray data to constrain the cut-off energy of the electron population. To reproduce the radio spectrum of Kes 79, we required an electron distribution with a power law index of $\alpha_e = 3.8$ and a magnetic field of 180 μG . The magnetic field required to model the radio spectrum of Kes 79 is larger than the average interstellar magnetic field (3–5 μG) and could arise from the magnetic fields being amplified by the shock-wave compressing the surrounding medium during the acceleration process.

If one makes reasonable assumptions about the fraction, ϵ , of total supernova explosion energy, E_{SN} , used to accelerated CRs, as well as the shock compression ratio, r , one can use this model to estimate the density of the surrounding medium with which the SNR shock wave is interacting. For this analysis, we set $r = 4$ and we assume that $\epsilon = 0.4$. This is a conservatively high estimate of the amount of supernova explosion energy expected to be converted into accelerating CRs. In Table 6, we summarize the estimated density of the γ -ray emitting material as well as the density of the X-ray emitting material derived in the literature and from our X-ray analysis.

When fitting the γ -ray spectrum of Kes 79 using a pion-decay model, we obtained a density of 14.5 cm^{-3} . This density is much larger than the values derived from the X-ray measurements listed in Table 5. This inferred density enhancement could indicate that the shock-wave of the SNR is interacting with cold, dense clumps of material (ISM or ejecta) that form due to instabilities in the post-shock flow (Castro & Slane 2010; Inoue et al. 2012). These cold dense clumps do not radiate significantly in X-rays. If these clumps of material have a high filling factor, then the densities inferred from the X-ray emission would significantly underestimate the local mean density. This scenario is consistent with a CO survey conducted by Scoville et al. (1987), which revealed a large elongated MC that overlaps the eastern and south eastern region of Kes 79. MCs are known to be clumpy in nature, with dense clumps of molecular material occupying only a fraction of the actual MC volume. This clumpy material can have a density of $n_H \sim 5\text{--}25 \text{ atoms cm}^{-3}$ (Chevalier 1999) or an ambient density of $n_0 \sim 1.25\text{--}6.25 \text{ cm}^{-3}$, if we assume $n_0 = n_H/4$. Our inferred ambient densities (Table 5) across the remnant fall within this range, supporting the original

conclusion that Kes 79 is interacting with a dense molecular material that does not radiate significantly in X-rays.

Alternatively, highly energetic particles accelerated by the remnant’s shock-wave could escape the acceleration region and stream ahead of the shock. These escaped particles can interact with the dense gas upstream of the shock, enhancing the detected γ -ray emission. A number of authors such as Aharonian & Atoyan (1996), Gabici et al. (2009), and Fujita et al. (2009) have shown that dense MCs in the vicinity of an SNR can significantly influence the γ -ray flux. However, the escaping particles in this scenario come predominantly from the higher energy part of the particle spectrum, leading to inconsistencies between the predicted and observed γ -ray spectrum.

4.3. Leptonic Origin of γ -rays

An alternative scenario is that the γ -ray emission coincident with Kes 79 arises from a non-thermal population of electrons in the form of IC or bremsstrahlung radiation. Bykov et al. (2000) and other authors have proposed this mechanism as the main production mechanism of γ -rays in SNRs. For completeness, we tested whether IC or non-thermal bremsstrahlung could be the dominant mechanism producing the γ -ray spectra of Kes 79. In order for the non-thermal bremsstrahlung to dominate the GeV γ -ray emission, the electron-to-proton ratio, K_{ep} , must be larger than ~ 0.2 (Gaisser et al. 1998). Local observations of the CR abundance ratio imply that $K_{\text{ep}} \sim 0.01$ (Gaisser et al. 1998), while models of the γ -ray emission from SNRs such as RX J1713.7–3946 suggest even smaller values of this ratio (Ellison et al. 2010).

Assuming that electrons make up approximately 1% of the relativistic particle energy budget (i.e., $K_{\text{ep}} = 0.01$), we determined that in order to reproduce the γ -ray spectrum of Kes 79, the total electron energy would be 1×10^{51} erg. This is equal to the entire canonical SN explosion energy, making it difficult to assert that IC is the dominant mechanism behind the γ -ray emission of Kes 79.

To test whether non-thermal bremsstrahlung is the dominant mechanism producing the γ -rays of Kes 79, we used the highest ambient density value derived in our X-ray analysis (see Table 5), as this would give us a lower limit on the total energy in accelerated electrons. Assuming $K_{\text{ep}} = 0.01$, we obtained a lower limit of 6.1×10^{50} erg for the total electron energy. This implies a total relativistic particle energy that is far in excess of the mechanical energy of an SNR. This fact makes it unlikely that non-thermal bremsstrahlung is the dominant mechanism behind the observed γ -rays of Kes 79.

5. CONCLUSION

In summary, using 52 months of *Fermi*-LAT data, we searched for γ -ray emission from SNR Kes 79, which is found to be interacting with MCs. Assuming that the main production mechanism for the observed γ -ray emission arises from pion decay, the inferred ambient density is high. This is consistent with observations of dense MCs near Kes 79. However, these estimates are

larger than the density derived from X-ray observations found in the literature. A pulsar association with the observed γ -ray emission is also considered for completeness as well as leptonic origin of the γ -ray emission. For Kes 79, an SNR origin of the emission is the most likely scenario, while a hadronic origin of the γ -rays was the most energetically favored mechanism. Additionally, we performed a spatial and spectral analysis of Kes 79 using 16 archival *XMM-Newton* observations and inferred an ambient density that is much smaller than the inferred ambient density from modeling the observed γ -ray emission. These results are consistent with scenarios represented by Castro & Slane (2010) and Abdo et al. (2009). We also performed a similar analysis for SNR Kes 78, but due to the uncertainties in the background γ -ray model or from γ -ray emission spilling over from nearby sources, we were unable to conclude that there is an excess of GeV γ -ray emission associated with this remnant.

The authors thank Dr. Thomas M. Dame for his in depth discussions in regards to the association and interaction of Kes 79 with its surrounding molecular cloud. K.A. thanks Dr. Jasmina Lazendic-Galloway for her helpful discussions in regards to the X-ray analysis. This work was partially funded by NASA grant NNX 11AQ096. P.S. acknowledges support from NASA contract NAS8-03060. D.C. acknowledges support for this work provided by NASA through SAO contract SV3-73016 to MIT for Support of the Chandra X-Ray Center, which is operated by the SAO under contract NAS8-03060.

REFERENCES

- Abdo, A., Ackermann, M., Ajello, M., et al. 2009, *ApJL*, **706**, L1
 Abdo, A., Ackermann, M., Ajello, M., et al. 2010a, *Sci*, **327**, 1103
 Abdo, A., Ackermann, M., Ajello, M., et al. 2010b, *ApJ*, **712**, 459
 Abdo, A., Ackermann, M., Ajello, M., et al. 2010c, *ApJS*, **187**, 460
 Abdo, A., Ackermann, M., Ajello, M., et al. 2011, *ApJ*, **734**, 28
 Abdo, A., Ajello, M., Allafort, A., et al. 2013, *ApJS*, **208**, 17
 Acciari, V. A., Aliu, E., Arlen, T., et al. 2011, *ApJL*, **730**, L20
 Ackermann, M., Ajello, M., Albert, A., et al. 2012, *ApJS*, **203**, 4
 Ackermann, M., Ajello, M., Allafort, A., et al. 2013, *Sci*, **339**, 807
 Aharonian, F. A., & Atoyan, A. M. 1996, *A&A*, **309**, 917
 Aliu, E., Arlen, T., Aune, T., et al. 2011, *Sci*, **334**, 69
 Allakhverdiev, A. O., Guseinov, O. K., Kasumov, F. K., & Iusifov, I. M. 1983, *Ap&SS*, **97**, 287
 Altenhoff, W. J., Downes, D., Goad, L., Maxwell, A., & Rinehart, R. 1970, *A&AS*, **1**, 319
 Anders, E., & Grevesse, N. 1989, *GeCoA*, **53**, 197
 Angerhofer, P. E., Becker, R. H., & Kundu, M. R. 1977, *A&A*, **55**, 11
 Aschenbach, B. 1998, *Natur*, **396**, 141
 Baring, M. G., Ellison, D. C., Reynolds, S. P., Grenier, I. A., & Goret, P. 1999, *ApJ*, **513**, 311
 Beard, M., & Kerr, F. J. 1969, *AuJPh*, **22**, 121
 Becker, R. H., & Kundu, M. R. 1975, *AJ*, **80**, 679
 Borkowski, K. J., Lyerly, W. J., & Reynolds, S. P. 2001, *ApJ*, **548**, 820
 Boumis, P., Xilouris, E., Alikakos, J., et al. 2009, *A&A*, **499**, 789
 Bykov, A., Chevalier, R., Ellison, D., & Uvarov, Y. 2000, *ApJ*, **538**, 203
 Case, G. L., & Bhattacharya, D. 1998, *ApJ*, **504**, 761
 Castro, D., & Slane, P. 2010, *ApJ*, **717**, 372
 Castro, D., Slane, P., Carlton, A., & Figueroa-Feliciano, E. 2013, *ApJ*, **774**, 36
 Castro, D., Slane, P., Ellison, D. C., & Patnaude, D. J. 2012, *AJ*, **756**, 88
 Castro, D., Slane, P., Patnaude, D. J., & Ellison, D. C. 2011, *ApJ*, **734**, 85
 Caswell, J. L., Clark, D., Crawford, D. F., & Green, A. J. 1975, *AuJPA*, **37**, 1
 Caswell, J. L., Milne, D. K., & Wellington, K. J. 1981, *MNRAS*, **195**, 89
 Caswell, J. L., Murray, J. D., Roger, R. S., Cole, D. J., & Cooke, D. J. 1975, *A&A*, **45**, 239
 Chen, Y., Jiang, B., Zhou, P., et al. 2013, arXiv:1304.5367
 Chen, Y., Zhang, F., Williams, R. M., & Wang, Q. D. 2003, *ApJ*, **595**, 227
 Chevalier, R. A. 1999, *ApJ*, **511**, 798
 Claussen, M., Frail, D., Goss, W. M., & Gaume, R. 1997, *ApJ*, **489**, 143
 Dickel, J. R. 1973, *AuJPh*, **26**, 369
 Dickel, J. R., & Denoyer, L. K. 1975, *AJ*, **80**, 437
 Dulk, P., & Slee, O. 1972, *AuJPh*, **25**, 429
 Ellison, D. C., Patnaude, D. J., Slane, P., & Raymond, J. 2010, *ApJ*, **712**, 287
 Frail, D. A. 2011, *MmSAI*, **82**, 703
 Frail, D. A., & Clifton, T. R. 1989, *ApJ*, **336**, 854
 Fujita, Y., Ohira, Y., Tanaka, S. J., & Takahara, F. 2009, *ApJL*, **707**, L179
 Gabici, S., Casanova, S., & Aharonian, F. A. 2009, in AIP Conf. Proc. 1085, High Energy Gamma-ray Astronomy, ed. F. A. Aharonian, W. Hofmann, & F. Rieger (Melville, NY: AIP), **265**
 Gaissner, T., Protheroe, R., & Stanev, T. 1998, *ApJ*, **492**, 219
 Giacani, E., Smith, M. J. S., Dubner, G., et al. 2009, *A&A*, **507**, 841
 Giordano, F., Naumann-Godo, M., Ballet, J., et al. 2012, *ApJL*, **744**, L2
 Giuliani, A., Cardillo, M., Tavani, M., et al. 2011, *ApJL*, **742**, L30
 Gosachinskii, I., & Khersonskii, V. K. 1985, *Ap&SS*, **108**, 303
 Gotthelf, E. V., Halpern, J. P., & Seward, F. D. 2005, *ApJ*, **627**, 390
 Green, A. J., Frail, D. A., Goss, W. M., & Otrupcek, R. 1997, *AJ*, **114**, 2058
 Green, D. A. 1989, *MNRAS*, **238**, 737
 Green, D. A., & Dewdney, P. E. 1992, *MNRAS*, **254**, 686
 Halpern, J. P., & Gotthelf, E. V. 2010, *ApJ*, **709**, 436
 Harrus, I. M., Slane, P. O., Smith, R. K., & Hughes, J. P. 2001, *ApJ*, **552**, 614
 Hewitt, J. W., Yusef-Zadeh, F., & Wardle, M. 2009, *ApJL*, **706**, L270
 Hnatyk, B., & Petruk, O. 1999, *A&A*, **344**, 295
 Inoue, T., Yamazaki, R., Inutsuka, S.-i., & Fukui, Y. 2012, *ApJ*, **744**, 71
 Kamae, T., Karlsson, N., Mizuno, T., Abe, T., & Koi, T. 2006, *ApJ*, **647**, 692
 Kassim, N. 1992, *AJ*, **103**, 943
 Kassim, N. E. 1989, *ApJS*, **71**, 799
 Kesteven, M. J. L. 1968, *AuJPh*, **21**, 369
 Koralesky, B., Frail, D., Goss, W. M., Claussen, M., & Green, A. J. 1998, *AJ*, **116**, 1323
 Kosack, K., Chaves, R. C. G., & Acero, F. 2011, in Proc. 32nd International Cosmic Ray Conference (ICRC2011), Vol. 7 (Beijing: IUPAP), 75
 Kovalenko, A. V., Pynzar', A. V., & Udalt'sov, V. A. 1994, *ARep*, **38**, 95
 Koyama, K., Petre, R., Gotthelf, E., et al. 1995, *Natur*, **378**, 255
 Kundu, M. R., & Velusamy, T. 1967, *AnAp*, **30**, 723
 Kuntz, K. D., & Snowden, S. L. 2008, *A&A*, **478**, 575
 Malkov, M. A., Diamond, P. H., & Sagdeev, R. Z. 2011, *NatCo*, **2**, 194
 Malkov, M. A., Diamond, P. H., & Sagdeev, R. Z. 2012, *PhPI*, **19**, 082901
 Malkov, M. A., & O'C Drury, L. 2001, *RPPh*, **64**, 429
 Manchester, R. N., Hobbs, G. B., Teoh, A., & Hobbs, M. 2005, *AJ*, **129**, 1993
 Mattox, J., Bertsch, D., Chiang, J., et al. 1996, *ApJ*, **461**, 396
 Mori, M. 2009, *Aph*, **31**, 341
 Morlino, G., & Caprioli, D. 2012, *A&A*, **538**, A81
 Nolan, P. L., Abdo, A. A., Ackermann, M., et al. 2012, *ApJS*, **199**, 31
 Park, S., Slane, P. O., Hughes, J. P., et al. 2007, *ApJ*, **665**, 1173
 Reynolds, S. P. 1998, *ApJ*, **493**, 375
 Reynolds, S. P. 2008, *ARA&A*, **46**, 89
 Saz Parkinson, P. M., & Fermi-LAT Collaboration, 2012, in AIP Conf. Proc. 1505, High Energy Gamma-ray Astronomy, ed. F. A. Aharonian, W. Hofmann, & F. M. Rieger (Melville, NY: AIP), **293**
 Scoville, N. Z., Yun, M. S., Sanders, D. B., Clemens, D. P., & Waller, W. H. 1987, *ApJS*, **63**, 821
 Seward, F. D., Slane, P. O., Smith, R. K., & Sun, M. 2003, *ApJ*, **584**, 414
 Slee, O. B. 1977, *AuJPA*, **43**, 1
 Stil, J. M., Taylor, A., Dickey, J., et al. 2006, *AJ*, **132**, 1158
 Sun, M., Seward, F. D., Smith, R. K., & Slane, P. O. 2004, *ApJ*, **605**, 742
 Sun, M., & Wang, Z. R. 2000, *AdSpR*, **25**, 549
 Tsunemi, H., & Enoguchi, H. 2002, *PASJ*, **54**, 735
 Uchiyama, Y., Aharonian, F. A., Tanaka, T., Takahashi, T., & Maeda, Y. 2007, *Natur*, **449**, 576
 Velusamy, T., Becker, R. H., & Seward, F. D. 1991, *AJ*, **102**, 676
 Vink, J. 2012, *A&ARv*, **20**, 49
 Warren, J. S., Hughes, J. P., Badenes, C., et al. 2005, *ApJ*, **634**, 376
 Wilms, J., Allen, A., & McCray, R. 2000, *ApJ*, **542**, 914
 Xu, J.-W., & Zhang, H.-R. 2009, arXiv:0909.0394
 Zhou, P., & Chen, Y. 2011, *ApJ*, **743**, 4
 Zubrin, S. Y., & Shulga, V. M. 2008, in Proc. 15th Young Scientists' Conference on Astronomy and Space Physics, ed. V. Y. Choliy & G. Ivashchenko (Kyiv: Kyivskiy Universitet), **41**